FULL PAPER

Sensors

ADVANCED
OPTICAL
MATERIALS
www.advopticalmat.de

Controlled Pinning of Conjugated Polymer Spherulites and Its Application in Detectors

Bernhard Dörling,* Antonio Sánchez-Díaz, Oriol Arteaga, Andrea Veciana, Maria Isabel Alonso, and Mariano Campoy-Quiles*

The nucleation of single macroscopic spherulites at desired positions, as well as ordered arrays of multiple spherulites, is demonstrated by combining the use of crystallizable solvents with local control of solvent evaporation during solution deposition. Moreover, the temperature assisted localized frustration of molecular orientation is shown, enabling the fabrication of samples containing both isotropic areas and spherulites. These macroscopic circular polycrystalline structures are characterized using a range of polarized spectroscopic techniques that allow quantifying their large degree of chain orientation. In order to show the potential of these large conjugated polymer spherulites centered at desired locations, graded bilayer organic photovoltaic devices were fabricated to be used as polarimeters, solid state light polarization detectors with no moving parts, and position sensitive photodetectors.

1. Introduction

Semiconducting polymers have been studied extensively in the last decades because of their remarkable optoelectronic properties and promising low-cost solution processability. From an engineering point of view, the precise control of the two related properties of crystallinity and orientation of polymers

B. Dörling, Dr. A. Sánchez-Díaz, A. Veciana,
Dr. M. I. Alonso, Dr. M. Campoy-Quiles
Institute of Materials Science of Barcelona (ICMAB-CSIC)
Campus of the UAB
Bellaterra 08193, Spain
E-mail: bdorling@icmab.es; mcampoy@icmab.es
Dr. O. Arteaga
Department of Applied Physics
Feman Group
University of Barcelona
08028 Barcelona, Spain
Dr. O. Arteaga
Institute of Nanoscience and Nanotechnology (IN2UB)
08028 Barcelona, Spain
A. Veciana
Science and Technology Faculty
University of Twente
7522 NB Enschede, The Netherlands

is of great interest because of their impact on mechanical, and functional properties, including thermal conductivity,[1] charge carrier mobility,[2–7] and electrical conductivity.[8,9] In addition, for suitable macroscopic polymer chain arrangements, polarized absorption and emission can be observed.[10] As a consequence, a variety of methods have been developed to manipulate and control the microstructure and the orientation of conjugated polymers.[11]

Some of these methods result in spherulites, densely branched, polycrystalline regions of material with spherically, or in 2 dimensions circularly, radiating fibers.[12,13]

Because of their circular shape, which contains all possible fiber orientations in the plane, spherulites are an attractive system to probe orientation-dependent electrical and optical properties. Conventional deposition techniques such as spin- and blade-coating usually result in isotropic layers with a random orientation of the crystalline lamellae down to the microscopic scale. This is caused by the immense density of nucleation sites and the resulting uncontrolled growth. Several methods to control the nucleation density have been demonstrated. For example, a careful control of the solvent partial pressure during swelling of an already deposited layer allows redissolving all but a few crystallites, which can then be regrown under controlled conditions to microscopic spherulites.[3,14] Another method, which is experimentally simpler to realize, uses the epitaxial growth of conjugated polymers or small molecules on crystalline 1,3,5-trichlorobenzene (TCB) from the melt,[15] or directly from solution,[16] resulting in larger macroscopic spherulitic structures. In the former, molten TCB acts as solvent for the conjugated system and upon reducing the temperature below the melting point, TCB solidifies, enforcing the epitaxial crystallization of the conjugated system. For the solution process, on the other hand, a given amount of TCB is mixed together with the conjugated component into a carrier solvent such as chlorobenzene (CB). During deposition at room temperature, the wet film dries, increasing the concentration of the solid content in the solution until the solubility limit is reached and the solutes start solidifying. In order to create oriented structures, TCB should crystallize before the polymer or small molecule, which defines a minimum TCB to polymer content (around 4% in volume for a 20 g L^{-1} P3HT solution in CB).[16]

The growth direction of spherulites can be controlled to some extent by patterning the substrate,[17] or by enforcing a

dominant drying direction.[18] However, to the best of our knowledge, controlling the initial location of nucleation during a conventional solution deposition process has thus far been elusive.[13] The difficulty arises from the stochastic character of the local composition fluctuations that result in the nucleation process, as well as the competition between nucleation and growth processes. Due to this lack of control, few applications make use of these otherwise interesting structures. For example, while multitudes of organic light detectors exist,[19] few are intrinsically polarization sensitive, even though there are many methods to prepare oriented layers of organic materials. Such detectors may incorporate conjugated polymers that have been oriented by rubbing,[20] or by stretching.[21,22] Similar functionality can be obtained from aligned carbon nanotubes.[23] Yet no method has been described for an easy solution-based process used to control the initial nucleation of spherulites, as described in this work.

The basic idea here introduced, is to control the drying locally using a flow of gas, and thus achieve the critical composition for TCB nucleation at the desired location, expediting the growth of a spherulite. Using this simple idea, samples comprising a single spherulitic structure, centered at the desired position and covering an area of about 4 cm^2, are demonstrated in this paper. The generalization to ordered arrays of spherulites is also shown. The presented method can be used to handily manufacture polarization sensitive photodetectors that allow to determine the intensity of incident light, as well as the angle and the degree of polarization, without requiring any moving parts. This could simplify the manufacturing of polarimeters with a wide range of applications, among them quality control,[24] or remote sensing.[25]

2. Results

2.1. Nucleation and Growth of a Single Spherulite

Thin film samples containing spherulites were prepared by deposition of a solution containing poly(3-hexylthiophene-2,5-diyl) (P3HT) and the additive TCB. As we have shown in a previous work, the density of nucleation centers which grow into macroscopic spherulites increases with higher weight ratio of TCB to P3HT and decreases with temperature.[18] As an example, a typical sample prepared with a ratio of 5:1, such as the one pictured in **Figure 1**a, contains ≈10 nucleation sites, resulting in up to cm^2-sized spherulites on a 25 by 25 mm^2 glass substrate. To prepare reproducible samples and devices, control over spherulite crystallization and over the precise location of initial nucleation is required, which so far has not been demonstrated.

Simple approaches, like modifying the substrate topography (e.g., by scratching) have no effect, while more complex methods, like engineering the substrate wettability, work somehow too well. They not only restrict the location of initial nucleation but also the further growth of spherulites.[17] It is this independent control of nucleation, without affecting growth, which we demonstrate in this work.

By carefully observing the drying process of a regular sample, one can conceive of a possible way to induce a preferential nucleation site. As can be inferred from Figure 1a, spherulites preferentially nucleate at the sample edges—at the
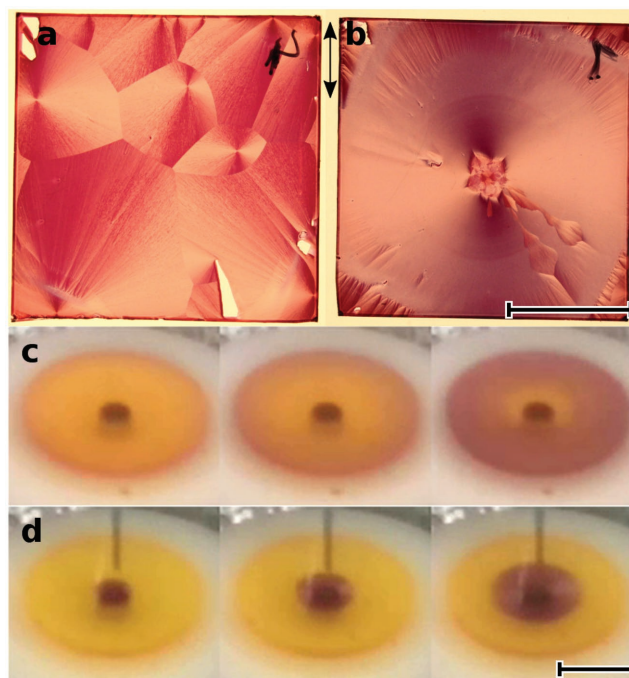

Figure 1. Spherulite samples and the drying process responsible for their formation during spin-coating. Samples can comprise a) several randomly nucleated spherulites, or b) a single centered one. c) The pair of three subsequent still images span 1 s during regular spin-coating, and d) 2 s while supplying a flow of gas through a needle visible above the substrate. The complete video is provided as Video S1 in the Supporting Information. Samples are illuminated from the back by vertically polarized light in panels (a) and (b). The scale bar is 10 mm.

contact line between the solution, the substrate, and the surrounding atmosphere. It is here, where the sample starts to dry first, locally increasing the concentration of the solid content, including the concentration of TCB, which is important in this case. This is recorded in Figure 1c for a sample during spin-coating. Noting that P3HT is orange in solution and purple in the dried film, it is clearly visible that the solvent first evaporates at the edges, and then proceeds towards the center of the sample, which remains in a dissolved state for the longest.

From the previous observation, it can be seen that spherulite nucleation sites appear where the film dries first and then grows from there. Therefore, one possible way to control the location of spherulites within a film is to speed up the evaporation of solvent at desired sites. For spin-coated samples, a single spherulite-like structure can be obtained when the sample starts drying at the center and proceeds outward from there. This way, nucleation can be confined to a single area that is much smaller than the final spherulite size, which is a significant improvement in nucleation control over the random nucleation at the contact line extended all along the substrate edge. A strategy to achieve the aforementioned central drying is by injecting a flow of gas through a needle pointing at the center of the substrate during spin-coating. Figure 1d shows consecutive still images of this process, clearly demonstrating that drying now starts at the center of the sample. The resulting sample is presented in Figure 1b, which shows a single spherulite-like structure. A complete video comparing both processes is provided as
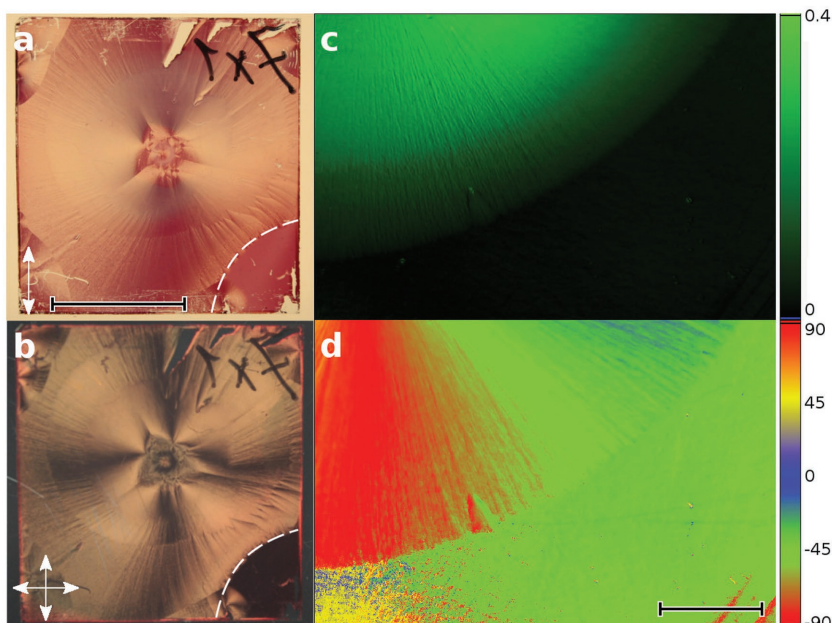
Figure 2. Local suppression of spherulite growth. a,b) Photographs of a sample that has been heated in the bottom right corner before deposition, inhibiting solidification of TCB. The sample is illuminated by vertically polarized light from the back (a), or placed between crossed polarizers (b). False-color Mueller-matrix images of c) the magnitude of the linear dichroism, and d) the orientation of the linear dichroism. Scale bars are 1 cm for the photos, and 1 mm for the images.

Video S1 (Supporting Information). For best results, care has to be taken to suppress any other, unwanted airflow in the environment during deposition.

2.2. Suppression of Spherulite Growth by Heating

Pure TCB has a melting point of 63 °C and stays liquid if sufficiently heated, acting like a regular high-boiling point solvent-additive that increases crystallinity by allowing for a longer lasting drying process.[26] Because TCB does not crystallize at elevated temperatures, it is not possible to use the local application of heat to control nucleation. Yet interestingly, combining a gas flow and heat allows to prepare samples that contain both isotropic and anisotropic regions, as depicted in **Figure 2**. The sample shown was fabricated as described in the previous section, the only difference being that one corner of the substrate was heated directly before deposition. As we will show, this capability can be of prime importance for a detector that measures the complete linear polarization of light. Figure S2 (Supporting Information) shows atomic force microscopy (AFM) measurements illustrating the differences in texture across the sample shown in Figure 2. Specifically, spherulitic regions may exhibit considerable surface roughness compared to isotropic regions.

2.3. Nucleation and Growth of an Array of Spherulites

To demonstrate the general viability of the presented method, a regular array of spherulites was grown on blade-coated

samples. One major difference between both spin- and blade-coating deposition methods is the speed at which the solvent evaporates. For a given temperature, solvent evaporates faster during spin-coating, due to the rotation of the sample. The additional flow of gas, that is employed to induce controlled nucleation, must be the dominating influence, surpassing any other, undesired airflow that may be present in a laboratory fume hood or glove box. Yet at the same time, the flow cannot be increased arbitrarily, since it will disturb the wet layer, physically displacing the solution on the substrate. In order to satisfy both of these conditions during the lengthy drying process of blade-coated samples, a 3D-printed array of nozzles pictured in **Figure 3** was manufactured. The concentric inlets and outlets serve to inject gas at the center of each inlet, while extracting it at the corresponding outlet. By confining the flow, each nozzle can be partially isolated from neighboring ones, providing circularly symmetric conditions at all nozzles. After coating of the sample, the nozzle array is placed above the still wet film, thus sealing any gaps beside the actual nozzles and preventing any unintended flow.

Figure 3c shows a photograph of a typical blade coated sample with 9 spherulites, that
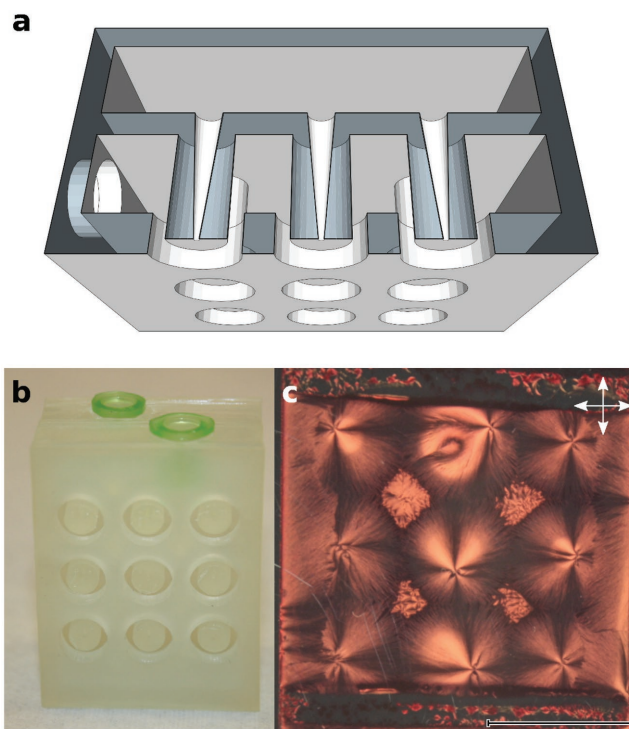

Figure 3. Spherulite array. a) Cross section of the design, as well as b) a photograph, of the nozzle array used to inject and extract gas, showing the two separate interior compartments. c) Photograph of a sample between crossed polarizers that contains 3 by 3 spherulites. The scale bar is 1 cm.

was prepared using this nozzle array. It is apparent that in addition to the forced drying process of the spherulites, the regular drying process, which starts at the edges of the sample, proceeds in parallel. Because of that, the growth of spherulites at the edge is disrupted by the regular drying process. However, since this process is restricted to the sample edges, it would be negligible if scaled up to larger samples. To further improve the results, an enhanced control over both the rate of injection as well as extraction is needed, ensuring truly identical conditions at all nozzle, completely isolating them from neighboring ones.

2.4. Optical Characterization

In order to understand the degree of orientation and crystallinity, as well as the different textures that are visible in the radial direction of the polarized photographs in Figures 1b and 2b, the samples were characterized using polarized photoluminescence (PL) spectroscopy, polarized Raman scattering, and ellipsometry. Complementary AFM data was also measured.

The dichroic ratio (DR) of the PL, the ratio of PL for excitation parallel versus perpendicular to the orientation direction, can be used to quantify the degree of orientation. An average value of $DR_{PL} = PL_{\parallel}/PL_{\perp} \approx 4$ at the wavelength of maximum PL around 700 nm was found for a representative sample, as calculated by averaging the polarized PL images shown in **Figure 4**.

Representative parallel and perpendicular spectra are shown in **Figure 5**a. These values confirm a large degree of orientation for a sample with the pinned nucleation center, comparable to values of DR = 3.77, observed in transmission, as shown in Figure S3 in the Supporting Information, and in line with earlier reports on samples deposited from solution with no control over nucleation position.[16] Right at the center, crystallites still have random orientation. Although the degree of orientation is large in the whole spherulitic structure, there are small (<20%) oscillating variations in DR_{PL} along the radius, which might be due to fluctuations in solid content as the drying front progresses along the liquid layer. These oscillations are correlated to the different textures observed radially, which arise from a change in the degree of misalignment of the fiber-like structures created during the epitaxial crystallization as seen in Figure S2 in the Supporting Information.[18] These fibrillar structures, which extend along the radial direction are not perfectly straight, but instead snake slightly back and forth. Correspondingly, the dichroic ratio is higher in regions where most of the fibers are parallel, compared to regions where they are less perfectly aligned. Sample thickness, which was determined by ellipsometry, is relatively homogeneous, ranging between 80 and 100 nm. Uniaxially oriented layers, which were obtained by pinning nucleation to the 1D contact line during blade-coating,[18] show a slightly lower dichroic ratio DR ≈ 3, which is in part due to the high surface roughness of the fibrillar layers, which contain a large volume of voids.

Polarized Raman also confirms a high degree of polymer orientation. The polarized Raman measurements in Figure 5b show a Raman dichroic ratio of $DR_{Raman} \approx 2.5$ at 488 nm excitation. Using this wavelength, the Raman signal comes from both amorphous and crystalline polymer chain segments.[27] The PL, on the other hand, arises preferentially from the crystalline segments due
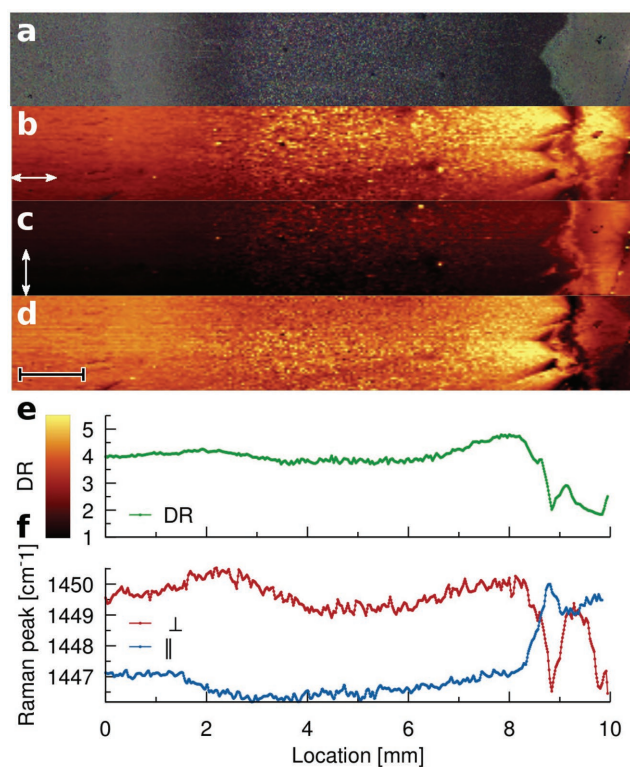

Figure 4. Optical characterization along the radial direction of a 10 mm long section of spherulite. a) Optical image, with the center of the spherulite located on the right. Map of the PL intensity for excitation b) parallel and c) perpendicular to the fibers. Calculated map of d) the dichroic ratio $DR = PL_{\parallel}/PL_{\perp}$ as well as e) averaged DR. f) Average of the Raman peak position along the sample. Scale bar represents 1 mm. Samples were excited at 532 nm.

to energy transfer toward the lowest lying energy level, known as selective PL. This, together with the specific dipole orientation of PL and Raman vibration, partially explains why $DR_{PL} > DR_{Raman}$. Reassuringly, the Raman dichroic ratio increases if exciting at a higher wavelength of 785 nm, which preferentially excites the crystalline chain segments, as seen in Figure 5c.

It has been shown that the Raman spectra of P3HT can provide information regarding the degree of crystallinity. Specifically, the peak centered at around 1450 cm^{-1} consists of the superposition of an amorphous component (peaking at higher energy) and a crystalline component (peaking at lower energy).[27] Therefore, a simple analysis of the center of mass of the convoluted peak can inform us about the degree of crystallinity. As shown in Figure 4f, the Raman peak for an excitation perpendicular to the orientation direction is shifted about 3 cm^{-1} toward higher energies with respect to parallel excitation, indicating that a higher ratio of amorphous polymer chains lies in perpendicular direction.[27] In regions where the formation of spherulites has been suppressed by an increased substrate temperature during deposition, this shift toward higher energy disappears, as shown in Figure S4 in the Supporting Information. Even though not oriented, this indicates that the frustrated regions have a high degree of crystallinity, similar to that of spherulites, as it is expected for P3HT films deposited from high boiling point solvents.[26]
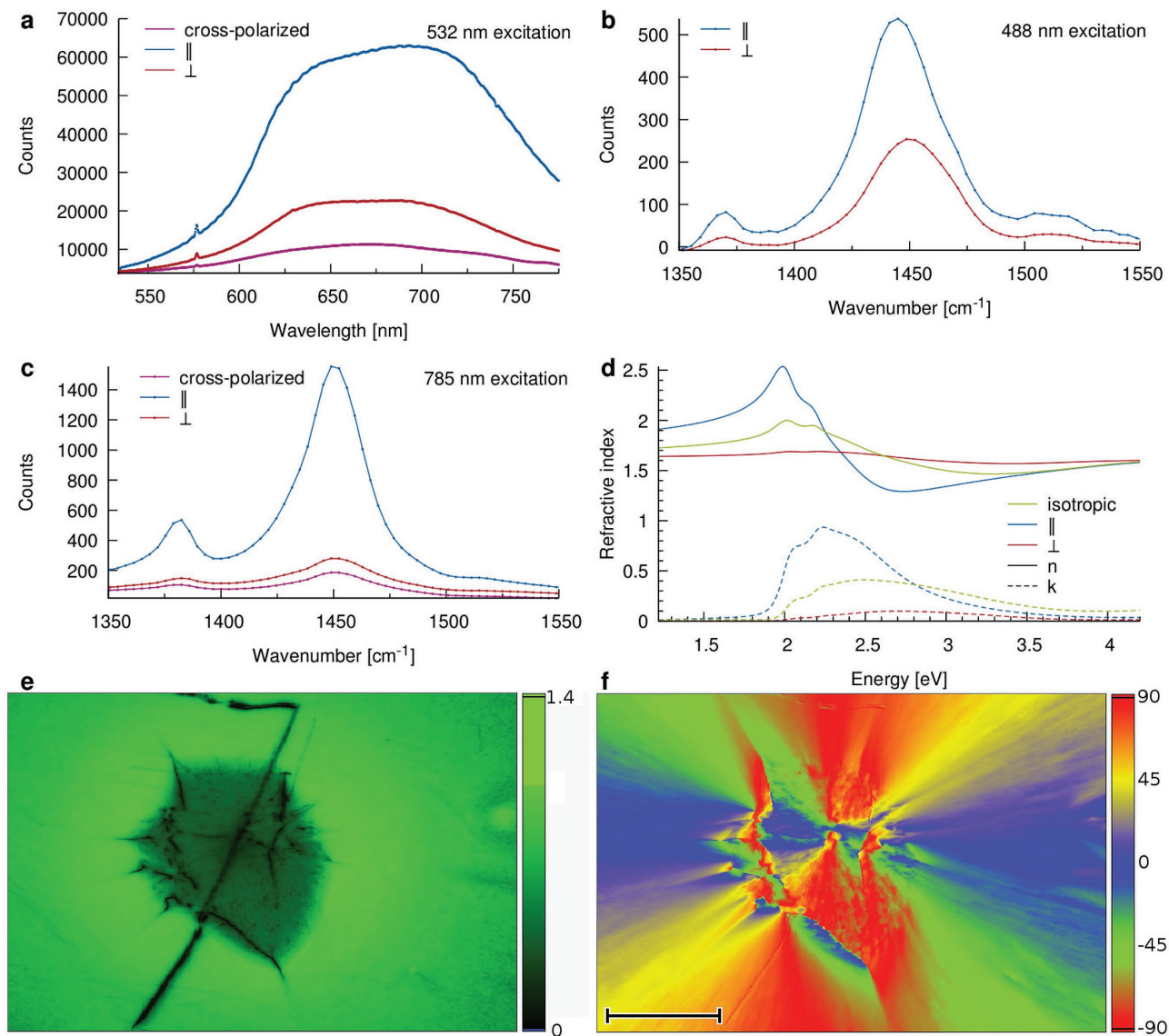
**ADVANCED
SCIENCE NEWS**
www.advancedsciencenews.com

**ADVANCED
OPTICAL
MATERIALS**
www.advopticalmat.de

Figure 5. Optical characterization of spherulites. a) Photoluminescence spectra for an excitation at 532 nm. Raman spectra for an excitation at b) 488 nm, and c) 785 nm. d) Complex refractive index of P3HT as determined by ellipsometry. Measured in an isotropic region where crystallization of TCB has been suppressed (yellow), and in a spherulitic region, using an anisotropic model with the extraordinary component (blue) parallel to the fiber direction and the ordinary component (red) perpendicular to the fiber direction. Mueller-matrix images of e) the magnitude, and f) the orientation of the linear dichroism. The scale bar corresponds to 1 mm.

Additional information regarding orientation and crystallinity can be obtained by looking at the absorption and refractive index, or in other words, the degree of dichroism and birefringence. Spectroscopic ellipsometry is a well-known technique for the determination of the complex refractive index of thin films and has here been used to characterize the real part (solid lines) and imaginary part (dashed lines) of a spherulitic sample, as plotted in Figure 5d. Details on the modeling are given in the Experimental Section. Pinned spherulitic films exhibit a strongly anisotropic complex refractive index. Absorption features are strongly pronounced for an excitation parallel to the orientation direction. Figure 5e,f shows false-color images for the magnitude and the orientation of the linear dichroism of a pinned P3HT spherulite, respectively. Figure 5e,f were

calculated from measurements using a Mueller-matrix microscope with an excitation wavelength of 532 nm, which is explained in more detail in the Experimental Section.

The shown orientation directly corresponds to that of the polymer chains, assuming that the transition dipole moment lies along the chain backbone. Figure 5e,f can serve to elucidate the process of spherulite formation. A comparatively isotropic region is located at the center of these pinned spherulites. Here, the abrupt solvent evaporation rapidly forms a dry film, not allowing for large-scale order. Along the contact line, around the circumference of this isotropic region, numerous nucleation sites form, from each of which a spherulite starts to grow in a space-filling manner. Competing with each other, they give the appearance of a single spherulite everywhere but

1700276 (5 of 10)

**ADVANCED
SCIENCE NEWS**
www.advancedsciencenews.com

**ADVANCED
OPTICAL
MATERIALS**
www.advopticalmat.de

the center. In the ideal case, the nucleation would be confined on a circle with infinitesimal circumference. However, mostly limited by the finite extension of the flow of gas, nucleation instead happens along a contact line that is neither a perfect circle nor infinitesimally short. In both the ideal as well as the real case, however, the nucleation itself still remains a stochastic process. Due to this remaining randomness, frontiers between neighboring spherulites can be visible in cases where the nucleation centers are distributed very irregularly along the contact line.

2.5. Application as Polarimeter

The capability to pin the nucleation of a spherulite at a desired location results in samples with predictable local orientation, opening the possibility to fabricate conceptually new types of devices. One example is a polarization detector with no moving parts (c.f. a conventional photodetector coupled to a rotating polarizer). Here, we demonstrate such a detector by producing organic photovoltaic (OPV) P3HT:PCBM graded bilayer devices. The P3HT layer contains a single, centered spherulite, which is covered by a [6,6]-phenyl C_{61} butyric acid methyl ester (PCBM) layer deposited from an orthogonal solvent. Fortunately, the orientation is retained upon deposition of PCBM and subsequent annealing, as evidenced by the barely affected dichroic ratio plotted in Figure S3 in the Supporting Information. Furthermore, Mueller-matrix images do not show any noticeable change upon deposition of PCBM, as shown in Figure S5 in the Supporting Information. Due to the radially distributed polymer chains, the electrical response of each cell depends on both the polarization of the incident irradiation as well as the intensity as a matter of course.

In order to detail the overall performance, **Figure 6**a shows the JV-characteristics of a device containing 8 cells under unpolarized illumination of 1 Sun. Average cell characteristics are summarized in **Table 1**, while Figure 6b shows the external quantum efficiency (EQE) of the highest performing cell.

Next, we evaluate the performance of devices like these as a polarimeter. **Figure 7**a shows the short circuit current density J_{sc} versus the angle of polarization of the incident light φ. A different device, with an average efficiency of only 0.8% was chosen, due to the particularly instructive character of its cells, as pictured in Figure 7b. Several facts are immediately apparent and serve to demonstrate the utility of the envisaged polarization sensor. Most importantly, the electrical response of each cell does indeed depend on the polarization, following the expected behavior given by Malus' law, proportional to $\cos^2(\varphi)$. Solid lines in Figure 7a are fits to

$$I_n = a_n \cos(\varphi - b_n)^2 + c_n \tag{1}$$

where c_n is a polarization insensitive offset (due to the nonoriented polymer chains) of cell n, b_n reflects the angle of preferential orientation for each cell, and a_n accounts for the dichroism-related photoresponse. The angle of maximum response b_n is different for each cell, since cells are distributed around the center of the spherulite, as pictured in Figure 7b. One cell exhibits a response that is essentially
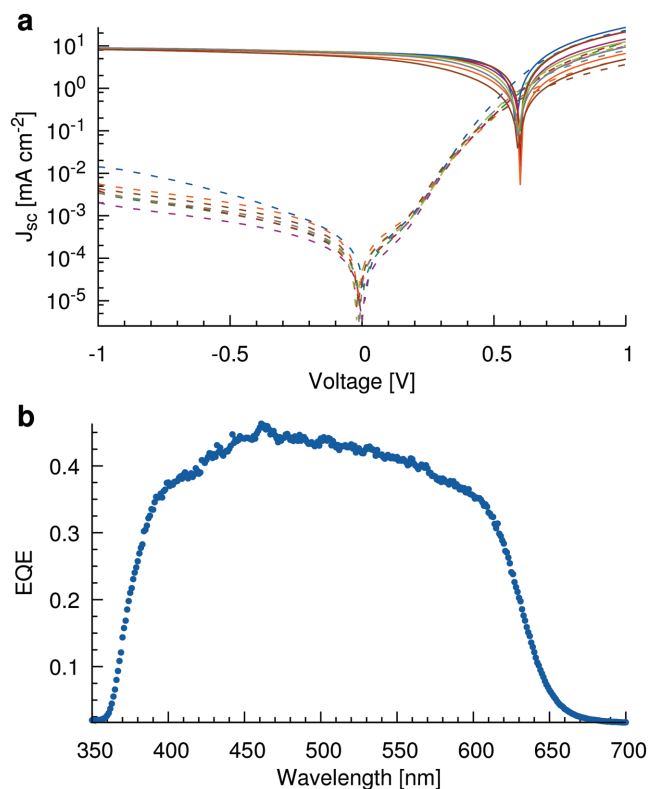

Figure 6. Electrical characterization under unpolarized light at 1 Sun. a) Dark and light JV-curves (dashed and solid lines, respectively) of the best graded bilayer OPV device with 8 cells. b) External quantum efficiency for the highest performing cell.

flat, independent of the polarization. As can be verified in Figure 7b, the reason for this is that most of the cell's active area is composed of isotropic polymer, not containing any spherulite.

This design has several advantages for applications as polarimeter. First, there are no moving parts, like in conventional polarimeters composed of a rotating linear polarizer placed in front of a polarization insensitive detector. This allows for faster measurements, which are not limited by the frequency of rotation of the polarizer.

Second, the accuracy in determining the polarization angle of incident light depends on the relative angle θ between polarizer and detector. Accuracy is poorest for angles when $\cos^2(\theta)$ has extreme values, i.e., when polarizer and detector are exactly parallel or perpendicular, since then the derivative is zero. This is normally circumvented by simultaneously measuring the response of several cells. Important in this case is the relative orientation of the individual cells to each other, not their absolute orientation. This is traditionally achieved by using several detectors, for example, four detectors based on

Table 1. Average device characteristics and standard deviation of 8 cells, as well as the values of the best performing cell in parenthesis.

V_{oc} [V]	J_{sc} [mA cm^{-2}]	FF [%]	h [%]
0.59 ± 0.01 (0.58)	6.4 ± 0.6 (6.99)	40 ± 7 (48)	1.55 ± 0.38 (1.96)

**ADVANCED
SCIENCE NEWS**
www.advancedsciencenews.com
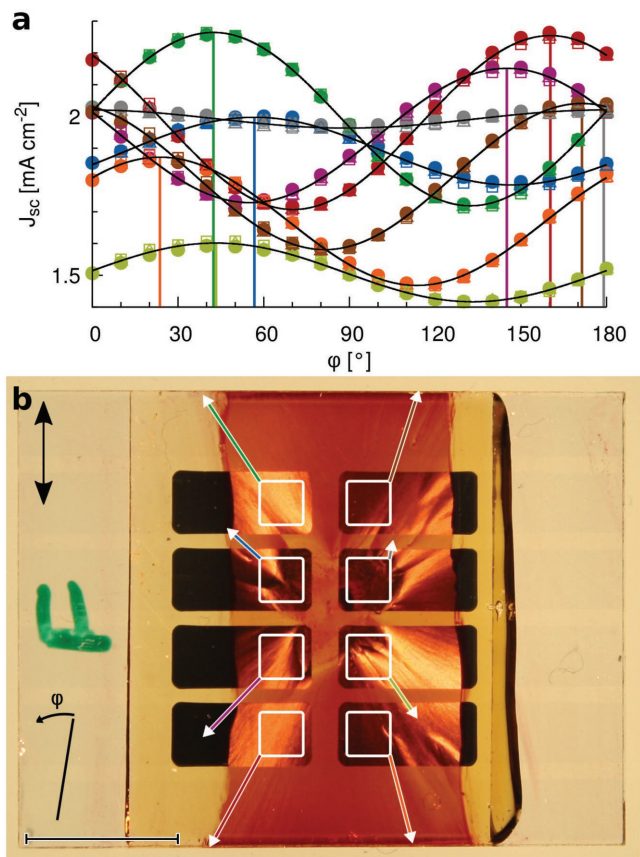
**ADVANCED
OPTICAL
MATERIALS**
www.advopticalmat.de

Figure 7. Electrical characterization under polarized light. a) Dependence of the short circuit current J_{sc} on the polarization angle φ of the incident light. As indicated, the maximum J_{sc} for each of the eight cells is obtained at a different angle of polarization. The plotted lines correspond to a fit of Equation (1). Open symbols represent measurements for angles $180° < \varphi < 540°$ to demonstrate reproducibility. b) Photograph of the glass-substrate side of the same device. The sample is illuminated by vertically polarized light from the back as well as unpolarized light from the front, to better reveal the spherulite on top of the aluminum cathode. All but the outlined white 1.6 by 1.6 mm^2 squares were masked during measurement. The arrows represent data extracted from the fits of panel (a) for the corresponding colors. The length of the arrow is proportional to the amplitude divided by the offset a_n/c_n, whereas the orientation corresponds to b_n measured counterclockwise (or $b_n + 180°$ for cells on the right side). The black line in the bottom left indicates $\varphi = 0° = 180°$. The scale bar is 5 mm.

wire-grid polarizers with relative orientation of 0°, 45°, −45°, and 90°. In our presented devices, this favorable relative orientation between cells is achieved by design, simply by placing individual cells along the circumference of a single spherulite, allowing for a simple fabrication. Furthermore, the number of cells can be easily changed as needed, potentially allowing for higher accuracy in an overdetermined system.

Figure S6 (Supporting Information) shows the parameters obtained from the fits of Figure 7 and their dependence on the bias voltage in more detail. The signal of interest is the ratio of the amplitude a_n divided by the offset c_n, which is used as a proxy for the detectivity of the polarization. This ratio does only slightly increase with increasing reverse bias voltage, whereas the angle b_n is not significantly influenced by the bias voltage.

Because of this, the proposed polarimeter could be used under zero-bias. Figure S7 (Supporting Information) shows similar plots, this time versus the incident irradiance. Satisfyingly, b_n does not depend on the light intensity, which allows for a simple calibration procedure of the proposed polarimeter.

The calibration procedure for the use of this device as a polarimeter consists in determining the coefficients a_n, b_n, and c_n for each of the 8 cells in one device. After calibration, the accuracy was estimated by predicting the polarization angle and irradiance of a test data set of 10 measurements, from the measured short circuit current using least squares fitting. On this data set, when using all 8 cells, the angles could be determined with a standard deviation of 2.7°, with a largest observed error of 6.4°. Similar results are obtained when using less cells, as long as cells are chosen that complement each other. Best results are obtained when selecting only a bare minimum of the best performing cells, in this particular case red, green, and gray, with a standard deviation of 0.5° and a largest observed error of 1° for the test data set. This error is of the same order than the estimated error due to the manual adjustment of the linear polarization during calibration, and compares well to other polarization sensitive organic devices, with errors of the order of 1%.[21,22] A video of the determination of the polarization and irradiance of light in real-time is provided as Video S8 in the Supporting Information.

A similar procedure than the one shown in the video has been used to determine the linear polarization of sunlight scattered by the sky. Since the polarization of scattered light depends on the position of the sun, our simple polarimeter can be used to determine the direction of the sun without directly observing the sun—in effect demonstrating a sundial that works in the shade.

2.6. Application as a Position Sensor

Another application that makes use of the polarization-dependent response is the determination of position along a single axis within a given cell. Previous position sensitive photodetectors based on organic materials rely on the resistivity of indium tin oxide (ITO),[28] on position-dependent changes of the transient response due to high device capacitance,[29] or on active layers having a thickness gradient.[30] In our case, we use the continuous change of orientation of a spherulite. Specifically, we take advantage of local changes of the angle of maximum absorption within a single extended cell. A position sensitive photodetector can be achieved by locally illuminating part of a cell with a small polarized light spot while monitoring the photocurrent. In our experiment, we used a 532 nm polarized laser, which was focused down to a spot size of 50 µm. As is observed in Figure 7, the measured local photocurrent depends on the polarization of the incoming light and is proportional to the local orientation of the spherulite. Because this local orientation changes throughout a cell, so does the photocurrent for a fixed polarization. A 2D photocurrent scan covering the whole purple cell from Figure 7, excited at four different angles of polarization, is shown in **Figure 8**a–d. These light-beam induced current (LBIC) maps were taken at increments of polarization of 45°. Using an average profile of

**ADVANCED
SCIENCE NEWS**
www.advancedsciencenews.com

**ADVANCED
OPTICAL
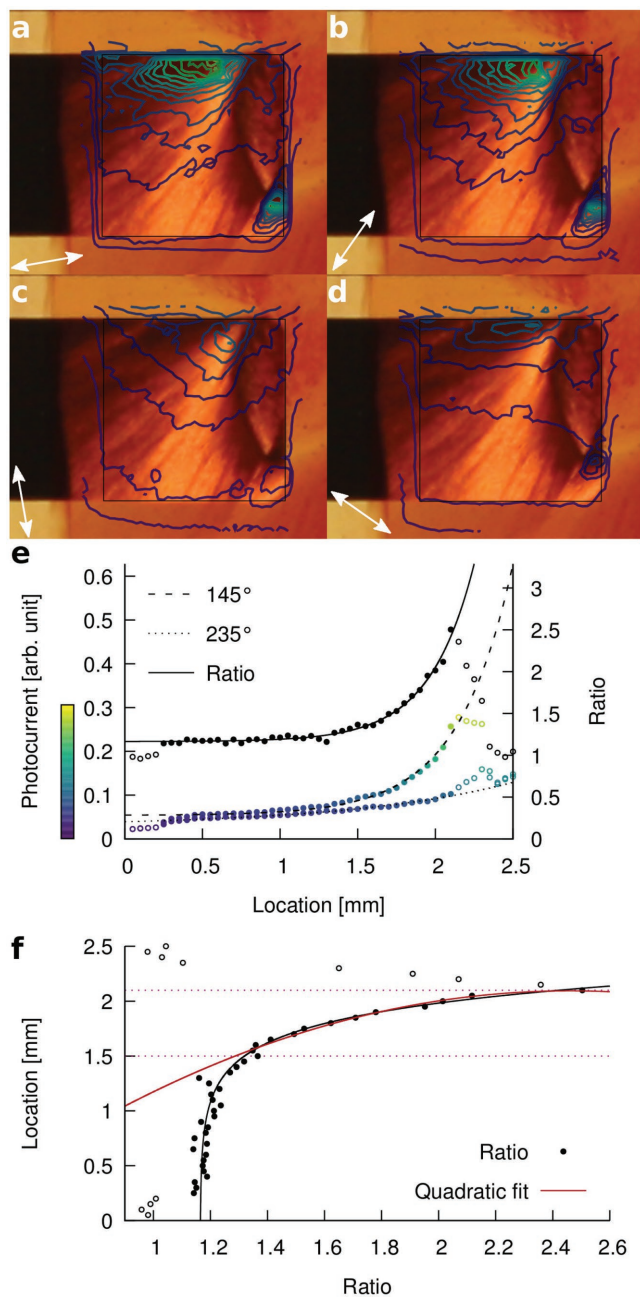MATERIALS**
www.advopticalmat.de

Figure 8. Dependence of photocurrent maps on polarization. a–d) LBIC maps of isophotocurrent for 532 nm excitation polarized at 100°, 145°, 190°, and 235°, respectively, for reference plotted on top a photograph of the corresponding cell (marked purple in Figure 7). e) Average profiles along the vertical direction, as well as their ratio. f) Quadratic fit to the inverse ratio.

these photocurrent maps along the vertical direction, shown in Figure 8e, the location of the light spot along one dimension can be determined from the photocurrent. This simple approach can be further improved, making it independent of light intensity, by instead considering the ratio of two photocurrent measurements at orthogonal polarizations. Figure 8f shows the inverse of this ratio as well as a quadratic fit used to parametrize the data, which allows to determine the location

with an estimated resolution of 100 µm, which is of the order of the used spot size. This is comparable to other organic detectors, with demonstrated resolutions ranging from about 600,[30] to 20,[28] and 12 µm.[29] Because of the small cell size of 2 by 2 mm² used in this study, an accurate detection of position is only possible along a relatively short distance of 0.6 mm. However, this distance can be increased by using longer electrode contacts and a suitably aligned spherulite.

3. Conclusions

We presented a facile solution-based method that allows to control the exact number and location of macroscopic P3HT spherulites using the crystallizable solvent TCB, and a spatial control over the evaporation rate obtained by localized gas flows. Furthermore, these spherulites can be deposited together with isotropic regions of material in a single step on the same substrate by controlled local heating. Using this method, we manufactured graded bilayer OPV devices with a polarization-dependent electrical response. These devices allow to determine 3 of the 4 Stokes parameters, and as such have applications as polarization sensitive photodetectors (polarimeters) and position sensitive photodetectors.

4. Experimental Section

Materials: P3HT ($M_w \approx 82$ kg mol^{-1}, $M_w/M_n \approx 2.4$, regioregularity >90%, Rieke Metals), CB, (CHROMASOLV 99.9%), dichloromethane (DCM, CHROMASOLV Plus >99.9%), and TCB (99%) were obtained from Sigma-Aldrich. PCBM (99%) was obtained from Solenne BV and poly(3,4-ethylenedioxythiophene)-poly-(styrenesulfonate) (PEDOT:PSS, Clevios P VP Al 4083) was purchased from Heraeus. Patterned ITO substrates, cover slides and UV-curable epoxy were purchased from Ossila. All materials were used as received.

Sample Preparation: P3HT was dissolved in CB at a concentration of 30 mg mL^{-1}. Typically, 150 mg mL^{-1} of TCB were added to this solution. PCBM was dissolved in DCM at a concentration of 10 mg mL^{-1}. ITO coated substrates with patterned electrodes and cut glass microscope slides were cleaned by consecutive sonications for 15 min in water with detergent, acetone, isopropanol, and finally in a solution of 10 wt% of NaOH in water, rinsing them with water after each step.

PEDOT:PSS was filtered using a 0.2 µm PVDF syringe filter, spin-coated at 3000 rpm, and annealed at 120 °C for 10 min. P3HT was spin-coated at 2500 rpm in a Laurell WS-400-6NPP-LITE spin-coater, or blade-coated on a Zehntner ZAA 2300 motorized stage at 20 mm s^{-1} with a ZUA 2000 blade set to a height of 200 µm. For some samples, a flow of gas of 2 mL s^{-1} was supplied through a flat-tipped needle with 0.8 mm diameter to induce controlled nucleation of a single spherulite.

The array of nozzles was 3D-printed with a Miicraft+ stereolithography printer with 100 µm feature size in z-direction and 7 s exposure per layer, using the resin BV-001 (model cream). Inlets have a diameter of 200 µm and a pitch of 8 mm. Blade-coated samples were prepared in two steps. First, a liquid film was deposited by passing the blade across the stationary substrate. Subsequently, the nozzle array was placed 1 mm above the wet sample by means of a spacer. The nine areas of controlled flow, each centered on an inlet, and circumscribed by an outlet, were sunk in by an additional millimeter by design. Gas was injected and extracted at rates of 10 mL min^{-1} using two NE 1000X syringe pumps from New Era Pump Systems, by applying positive and negative pressure to the inlet and outlet, respectively. The flows were maintained for several minutes, until the samples were dried.

**ADVANCED
SCIENCE NEWS**
www.advancedsciencenews.com

**ADVANCED
OPTICAL
MATERIALS**
www.advopticalmat.de

Additionally, to inhibit the nucleation of TCB, some samples were partially placed on a hotplate heated to 70 °C for several seconds. PCBM solution was filtered using a 0.22 μm PTFE syringe filter and spin-coated at 4000 rpm. DCM is a bad solvent for P3HT, allowing for sufficient diffusion of PCBM into the P3HT layer, yet not dissolving it during deposition.[26] Samples were annealed at 120 °C for 10 min in a nitrogen filled glove box, before thermally evaporating 100 nm of aluminum to form the cathode. Afterward, finished samples were annealed again at 140 °C for 10 min in inert atmosphere to further diffuse the PCBM into the P3HT layer, forming a diffusive bilayer with a gradual change in composition. These graded bilayers of P3HT and PCBM had an average thickness of 160 nm, as determined by AFM. Subsequently, samples were encapsulated using UV curable epoxy and a glass cover slide.

For optical characterization, P3HT was deposited directly onto cleaned glass substrates, and stored in a desiccator overnight to sublimate the TCB.

Sample Characterization: Photovoltaic performance was characterized using a AAA Solar Simulator conforming to the AM1.5G spectrum (SAN-EI Electric, XES-100S1). Irradiation was calibrated to 1000 W m^{-2} using a NREL certified Si reference cell (Oriel Instruments, 91150V). For polarized measurements, a linear polarizer (Thorlabs, LPVISE200-A) on a rotatable mount was interposed in the light path, lowering the irradiation to ≈ 575 W m^{-2}. Individual cells had an area of 2 by 2 mm^2 and were covered by a shadow mask with 1.6 by 1.6 mm^2 sized holes during measurement. Before the measurement, samples were exposed for 1 h to irradiation of 1000 W m^{-2}, in order to burn in and stabilize subsequent performance.

EQE was measured using a custom-built setup. Light from a xenon lamp was passed through a monochromator (Horiba microHR). Using a beamsplitter (Thorlabs BPD254-G), this light then simultaneously illuminated the sample and a photodiode connected to a power meter (Thorlabs S120VC & PM100A). Current was acquired using a multimeter (Keithley 2400 SourceMeter).

Light-beam induced current was measured on a custom-made system. The sample was located on a motorized X, Y, and Z stage, and illuminated locally by a 532 nm laser (Thorlabs, CPS532). After passing through a multimode optical fiber and a beamsplitter (Thorlabs, EBS1), the laser was again polarized using a linear polarizer (Thorlabs, LPVISE200-A). Light was focused on the device using a long working distance 20× Mitutoyo objective. The incident light intensity was monitored with a photodiode power sensor (Thorlabs, S120VC) connected to a digital power meter (Thorlabs, PM100D). The short circuit current was monitored with a multimeter (Keithley 2400 SourceMeter). Data was acquired using a custom software, which allowed to keep the sample plane in focus and the diameter of the laser spot below 30 μm.

Photographs were taken using a Canon EOS 1000D camera, by illuminating samples from the back and placing them on a single, or between two crossed polarizer sheets (Thorlabs, LPVISE2 × 2).

Polarized photoluminescence and Raman scattering images were acquired using a WITec alpha300 RA confocal Raman microscope. The samples were placed on a combined step motor/piezo stage and excited through a 10× objective using solid state lasers centered at 488 and 785 nm. Images were analyzed using WITec Project FOUR software.

Space-resolved Mueller-matrix measurements based on the transmission of light through the spherulites were done with a custom-made Mueller-matrix microscope that has been described in detail elsewhere.[31,32] The basic optical design of the instrument is based on a commercial Carl-Zeiss JENAVAL polarization microscope and it allows for measurements at different levels of magnification and wavelength. Briefly, this instrument works by frequency-analyzing the intensity of light captured at every pixel of a camera detector, while two rotating film compensators, one placed before the sample and the other one after it, continuously modulate the polarization of light with two distinct frequencies. The Mueller-matrix captured at each pixel of the image can then be processed to calculate, among others, the linear birefringence and linear dichroism at that point of the sample with a simple analytic formalism.[33,34]

The spectroscopic values of the linear birefringence and linear dichroism were measured in transmission with a Mueller-matrix polarimeter.[35] The spot size had a diameter of ≈0.8 mm so that different parts of the spherulite could be selected for measurement.

Spectroscopic ellipsometry was measured with a Sopralab GES5E rotating polarizer ellipsometer with a focused spot size of ≈200 μm. Based on the images of linear dichroism and linear birefringence, we measured at several points with the plane of incidence of light oriented parallel or perpendicular to the directions of largest absorption or refraction, which coincide with the directions along or perpendicular to the fibers. Within the experimental error, the anisotropic optical response is uniaxial with a variable in-plane optic axis aligned with the fibers.[36] Thus, the extraordinary components n_e and k_e are high and the ordinary ones n_o and k_o are low. Accordingly, the ellipsometric spectra were analyzed by combining pairs of spectra measured in the two described configurations to evaluate the film thickness and the n and k parameters of the uniaxial films. The spectra vary from point to point due to changes in thickness, roughness, and crystallinity. From these, the thickness seems to be rather constant. In order to obtain a reliable description of the spectral optical anisotropy, the ellipsometric and polarimetric results were combined. For further details regarding the ellipsometric characterization, see Note S9 in the Supporting Information.

Supporting Information

Supporting Information is available from the Wiley Online Library or from the author.

Acknowledgements

Conflict of Interest

The authors declare no conflict of interest.

Keywords

[1] S. Shen, A. Henry, J. Tong, R. Zheng, G. Chen, *Nat. Nanotechnol.* **2010**, *5*, 251.

[2] L. H. Jimison, M. F. Toney, I. McCulloch, M. Heeney, A. Salleo, *Adv. Mater.* **2009**, *21*, 1568.

[3] E. Crossland, K. Tremel, F. S. U. Fischer, K. Rahimi, G. Reiter, U. Steiner, S. Ludwigs, *Adv. Mater.* **2012**, *24*, 839.

[4] A. Luzio, L. Criante, V. D'Innocenzo, M. Caironi, *Sci. Rep.* **2013**, *3*, 3425.

[5] N.-K. Kim, S. Jang, G. Pace, M. Caironi, W.-T. Park, D. Khim, J. Kim, D. Kim, Y. Noh, *Chem. Mater.* **2015**, *27*, 8345.

[6] S. G. Bucella, A. Luzio, E. Gann, L. Thomsen, C. R. McNeill, G. Pace, A. Perinot, Z. Chen, A. Facchetti, M. Caironi, *Nat. Commun.* **2015**, *6*, 8394.

[7] N. Martino, D. Fazzi, C. Sciascia, A. Luzio, M. R. Antognazza, M. Caironi, *ACS Nano* **2014**, *8*, 5968.

[8] T. Takano, H. Masunaga, A. Fujiwara, H. Okuzaki, T. Sasaki, *Macromolecules* **2012**, *45*, 3859.

[9] N. Kim, S. Kee, S. H. Lee, B. H. Lee, Y. H. Kahng, Y.-R. Jo, B.-J. Kim, K. Lee, *Adv. Mater.* **2014**, *26*, 2268.

[10] M. Grell, D. D. C. Bradley, *Adv. Mater.* **1999**, *11*, 895.

[11] M. Brinkmann, L. Hartmann, L. Biniek, K. Tremel, N. Kayunkid, *Macromol. Rapid Commun.* **2014**, *35*, 9.

[12] L. Gránásy, T. Pusztai, T. Börzsönyi, J. A. Warren, J. F. Douglas, *Nat. Mater.* **2004**, *3*, 645.

[13] L. Gránásy, L. Rátkai, A. Szállás, B. Korbuly, G. I. Tóth, L. Környei, T. Pusztai, *Metall. Mater. Trans. A* **2014**, *45*, 1694.

[14] E. Crossland, K. Rahimi, G. Reiter, U. Steiner, S. Ludwigs, *Adv. Funct. Mater.* **2011**, *21*, 518.

[15] M. Brinkmann, J. C. Wittmann, *Adv. Mater.* **2006**, *18*, 860.

[16] C. Müller, M. Aghamohammadi, S. Himmelberger, P. Sonar, M. Garriga, A. Salleo, M. Campoy-Quiles, *Adv. Funct. Mater.* **2013**, *23*, 2368.

[17] S. S. Lee, S. B. Tang, D.-M. Smilgies, A. R. Woll, M. A. Loth, J. M. Mativetsky, J. E. Anthony, Y.-L. Loo, *Adv. Mater.* **2012**, *24*, 2692.

[18] B. Dörling, V. Vohra, T. Thanh Dao, M. Garriga, H. Murata, M. Campoy-Quiles, *J. Mater. Chem. C* **2014**, *2*, 3303.

[19] K. J. Baeg, M. Binda, D. Natali, M. Caironi, Y. Y. Noh, *Adv. Mater.* **2013**, *25*, 4267.

[20] R. Zhu, A. Kumar, Y. Yang, *Adv. Mater.* **2011**, *23*, 4193.

[21] S. G. Roy, O. M. Awartani, P. Sen, B. T. O'Connor, M. W. Kudenov, *Opt. Express* **2016**, *24*, 14737.

[22] R. Yang, P. Sen, B. T. O'Connor, M. W. Kudenov, *Appl. Opt.* **2017**, *56*, 1768.

[23] L. Zhang, Y. Wu, L. Deng, Y. Zhou, C. Liu, S. Fan, *Nano Lett.* **2016**, *16*, 6378.

[24] N. A. Hagen, D. S. Sabatke, J. F. Scholl, P. A. Jansson, W. W. Chen, E. L. Dereniak, D. T. Sass, *Proc. SPIE* **2003**, *5158*, 45.

[25] J. S. Tyo, D. L. Goldstein, D. B. Chenault, J. A. Shaw, *Appl. Opt.* **2006**, *45*, 5453.

[26] V. Vohra, B. Dörling, K. Higashimine, H. Murata, *Appl. Phys. Express* **2016**, *9*, 12301.

[27] W. C. Tsoi, D. T. James, J. S. Kim, P. G. Nicholson, C. E. Murphy, D. D. C. Bradley, J. Nelson, J.-S. Kim, *J. Am. Chem. Soc.* **2011**, *133*, 9834.

[28] B. P. Rand, J. Xue, M. J. Lange, S. R. Forrest, *IEEE Photonics Technol. Lett.* **2003**, *15*, 1279.

[29] A. P. Arndt, S. W. Kettlitz, J. Mescher, U. Lemmer, *IEEE Photonics Technol. Lett.* **2016**, *28*, 617.

[30] J. Cabanillas-Gonzalez, O. Peña-Rodríguez, I. Suarez Lopez, M. Schmidt, M. I. Alonso, A. R. Goñi, M. Campoy-Quiles, *Appl. Phys. Lett.* **2011**, *99*, 103305.

[31] O. Arteaga, M. Baldrís, J. Antó, A. Canillas, E. Pascual, E. Bertran, *Appl. Opt.* **2014**, *53*, 2236.

[32] E. Kuntman, O. Arteaga, J. Antó, D. Cayuela, E. Bertrán, *Opt. Pura Apl.* **2015**, *48*, 309.

[33] O. Arteaga, A. Canillas, *Opt. Lett.* **2010**, *35*, 559.

[34] O. Arteaga, A. Canillas, *Opt. Lett.* **2010**, *35*, 3525.

[35] O. Arteaga, J. Freudenthal, B. Wang, B. Kahr, *Appl. Opt.* **2012**, *51*, 6805.

[36] M. Campoy-Quiles, M. I. Alonso, D. D. C. Bradley, L. J. Richter, *Adv. Funct. Mater.* **2014**, *24*, 2116.

1700276 (10 of 10)